Determination of yield stress of 2D (Yukawa) dusty plasma

Bin Liu and J. Goree
Department of Physics and Astronomy, The University of Iowa, Iowa City, Iowa 52242, USA

(Received 7 July 2017; accepted 29 August 2017; published online 19 September 2017)

Elastic and plastic deformations of a two-dimensional (2D) dusty plasma crystal under shear stresses are investigated using a numerical simulation. Our simulation mimics experiments that start with a crystal that is then manipulated by a pair of laser beams separated by a gap. In a pair of rectangular regions, we apply two equal but oppositely directed forces, to induce a shear deformation in the gap between. These external forces are increased incrementally to examine the elastic behavior, plasticity, and liquid flows. In the low-force elastic limit, a measurement of the shear modulus is obtained, which agrees with a theoretical value based on a sound speed. For larger forces resulting in plastic deformation, we determine the yield stress, which is found to agree with a common theoretical model for the critical yield stress, after accounting for the dimensionality for 2D. *Published by AIP Publishing*. [http://dx.doi.org/10.1063/1.4994840]

I. INTRODUCTION

Strongly coupled plasmas (SCPs) can exhibit liquid-like or solid-like properties. Such an SCP is characterized by an interparticle potential energy that greatly exceeds the kinetic energy of the constituent charged particles. The parameter for describing the coupling is

$$\Gamma \equiv \frac{Q^2}{4\pi\epsilon_0 a k_B T_p}, \tag{1}$$

where Q is the particle charge, a is the particle spacing characterized by the Wigner-Seitz radius,[1] and T_p is the kinetic energy of particles. In response to shear stresses, an SCP can deform or flow. If the SCP is already in a liquid state, its response to shear stress is a flow pattern called shear flow, which has been investigated in simulations[2–4] and experiments.[5–8] Here, instead of a liquid, we investigate the response starting with an SCP in a solid state.

The SCP in this study is dusty plasma. Dusty plasmas have four constituents: electrons, ions, neutral gas, and micron-size particles of solid matter.[9–21] These solid particles, which are often called dust particles, carry a large negative charge. A collection of dust particles can be electrically confined into a three-dimensional (3D) cloud or a two-dimensional (2D) layer. In either case, the space between dust particles is filled by electrons and ions, which modify the usual $1/r$ scaling by the effect of screening. The interaction is often approximated as a (Yukawa) potential[22]

$$\phi(r) = \frac{Q^2}{4\pi\epsilon_0}\frac{e^{-r/\lambda_D}}{r}, \tag{2}$$

where λ_D is the screening length. For dust particles in a 2D plane, the Yukawa potential is consistent with the experimental observation.[23] Ion wake effects, which are not included in Eq. (2), can affect the potential especially by giving it an anisotropic character that can play a large role in a 3D cloud.[24,25] The effects of ion wakes are much less profound for a 2D cloud.

When it has solid-like properties, a strongly coupled dusty plasma is extremely soft. As a measure of softness, it has been noted that the shear modulus of 3D dusty plasma solids is about 10^{19} times smaller than for metals,[15,26] and 10^6 times smaller than for colloidal crystals.[26,27] This small modulus allows very large deformation with only a small applied force, even for a force as small as 10^{-14} N, as can be applied by a manipulation laser. Manipulation lasers have been used to apply an external force in several experiments in the PK-4 instrument, which is on orbit on the International Space Station (ISS),[28] and in the laboratory. Laboratory experiments using manipulation lasers in 2D dusty plasmas have been reported for studying deformation,[29–33] melting,[34] viscoelastic response,[35] and shear flows.[5–8,36,37] Plastic deformation was studied by Durniak and Samsonov[29,31] using compression, and by Hartmann *et al.*[32] using shear.

In this paper, we study the elastic and plastic deformations of a 2D dusty plasma crystal using a numerical simulation. We use realistic experimental parameters, and to mimic experiments with manipulation lasers, we apply shear forces in two rectangular regions, separated by a gap. We analyze particle position, velocity, and interparticle force data to obtain the stress as well as the strain. Based on the stress-strain relationship, we empirically characterize the elasticity and plasticity of 2D dusty plasmas. The previous work on the elastic properties included a report of shear modulus, without units.[38] Here we report results not just for shear modulus but also for yield stress, in both physical and dimensionless units.

Here we briefly review the concepts of shear stress, shear strain, and stress-strain relationship. Shear stress arises from a force applied along a sample's edge (although a dusty plasma allows applying such a force in the center of the sample). The shear stress is the force divided by the area or length of the edge, for 3D and 2D samples, respectively. The strain is the response to the shear stress. Strain γ is a dimensionless measure of deformation; it is defined as the ratio of the change in length to a reference length. For the configuration sketched in Fig. 1(a), the reference length is the gap width, and γ is the tangent of the angle for the deformation of the sample.

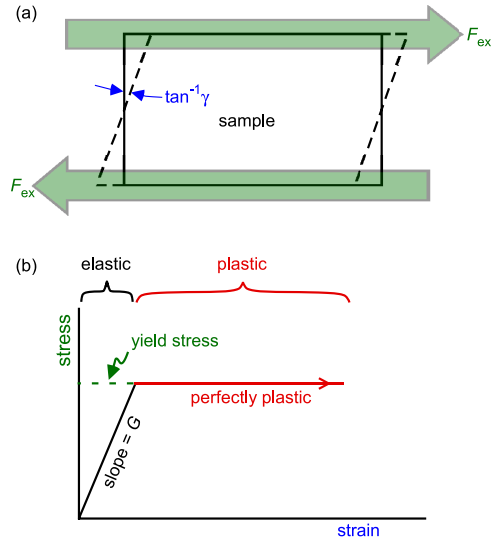

FIG. 1. Illustration of concepts. (a) External shearing forces F_{ex} cause a stress and a strain γ, within a gap between the two force regions. (b) Sketch of the stress-strain relationship. In an experiment, if a fixed level of stress is applied to a sample, the response will be different in two regimes: for elastic deformation the strain will remain constant (at some fixed point along the sloped line, in the elastic limit), while for plastic deformation the strain will gradually increase with time (following the horizontal line to the right). The yield stress marks the end of the elastic limit and the onset of plastic deformation.

The variation of strain γ with stress τ shows generally two distinctive regimes, as sketched in Fig. 1(b). At small strains, the substance is in its elastic limit, where stress and strain are linearly related by,

$$\tau = G\gamma, \tag{3}$$

where G is the shear modulus. At large strains, on the other hand, the substance undergoes plastic deformation, with a stress that varies less with strain than in the elastic limit. In the case of perfectly plastic deformation, the stress varies not at all with strain. The stress at the onset of plastic deformation is termed the yield stress. These macroscopic variables, stress and strain, are observables for all kinds of materials including granular materials,[39,40] colloids,[27,41] and many other complex fluids.[42,43]

II. METHOD

A. Langevin dynamics simulation

A Langevin dynamics simulation was performed by integrating the equation of motion

$$m_p\ddot{\mathbf{r}}_i = -\sum_j \nabla\phi_{ij} - \nabla\Phi - \nu_{\rm gas} m_p\dot{\mathbf{r}}_i + \boldsymbol{\zeta}_i(t) + \mathbf{F}_{\rm ex}, \tag{4}$$

for a particle i of mass m_p. The five force terms on the right-hand side of Eq. (4) describe the particle-particle interaction, confining potential, gas drag, Langevin random kicks, and an external manipulation to apply a stress. We integrated the equation of motion for $N = 4096$ particles. The boundary conditions were periodic in the x direction, which is the direction of $\mathbf{F}_{\rm ex}$, while in the y direction, particles were confined by the potential Φ in the same manner as in Ref. 44.

The initial configuration of the simulation was in a solid state, with experimentally relevant parameters. We chose $\Gamma = 800$ and $a/\lambda_D = 0.73$, and under these conditions, particles self-organized in a lattice structure. A high degree of spatial order can be seen in the map of particle position, Fig. 2, where it is evident that there were three crystalline domains, and in the pair correlation function $g(r)$, Fig. 3(a). The presence of multiple domains probably had a little effect on our conclusions because all the further results we will present are an analysis within the central gap, where initially there was only one domain.

The simulation parameters were based on the experiment of Ref. 5. We assumed that the microspheres had a diameter of 8.7 μm, a mass $m_p = 5.2 \times 10^{-13}$ kg, a number density $n_{2D} = 4.1\,\mathrm{mm}^{-2}$, and a charge $Q = -15000$ e. The screening length and particle spacing were comparable, $\lambda_D = 380\,\mu$m and $a = 1/\sqrt{n_{2D}\pi} = 280\,\mu$m, respectively. The friction constant was $\nu_{gas} = 1.1\,\mathrm{s}^{-1}$, assuming argon gas pressure of 6

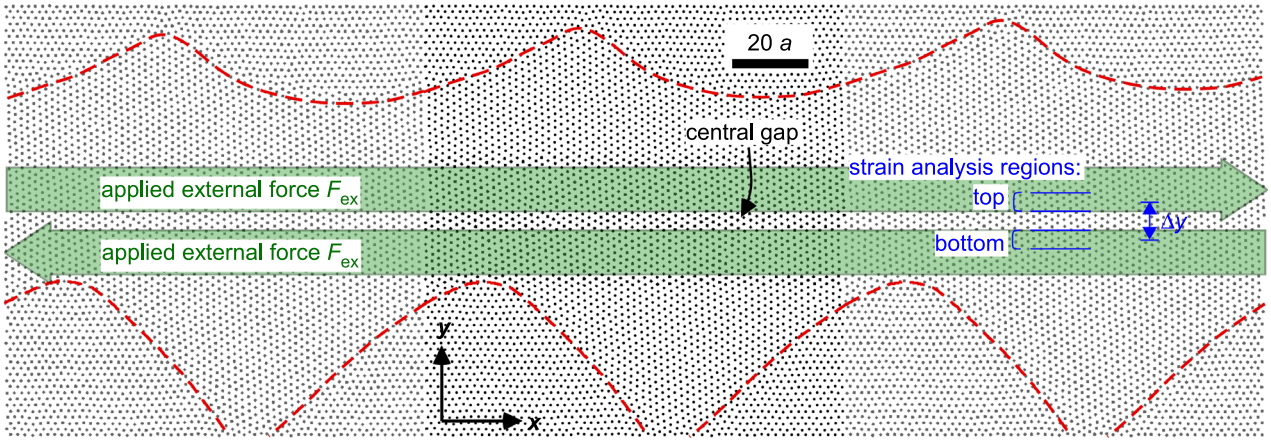

FIG. 2. Simulation of shear deformation of 2D dusty plasma under external stresses. In the x direction, periodic boundary conditions are used, as indicated by the two image cells of the central square. In the y direction, there is a confining potential, localized to the edge, with a parabolic spatial profile. The initial conditions, shown here, have a particle arrangement that is crystalline, with three domains separated by domain walls indicated by dashed lines. External manipulation is exerted beginning at $t = 0$ in the two shaded regions (imitating laser beams in an experiment) by applying a uniform force F_{ex} within these regions. Results shown will be mostly for the central gap, between the regions of the applied forces. In our analysis, to obtain the shear strain, we find the average particle displacement in two analysis regions, which are slices at the top and bottom of the central gap.

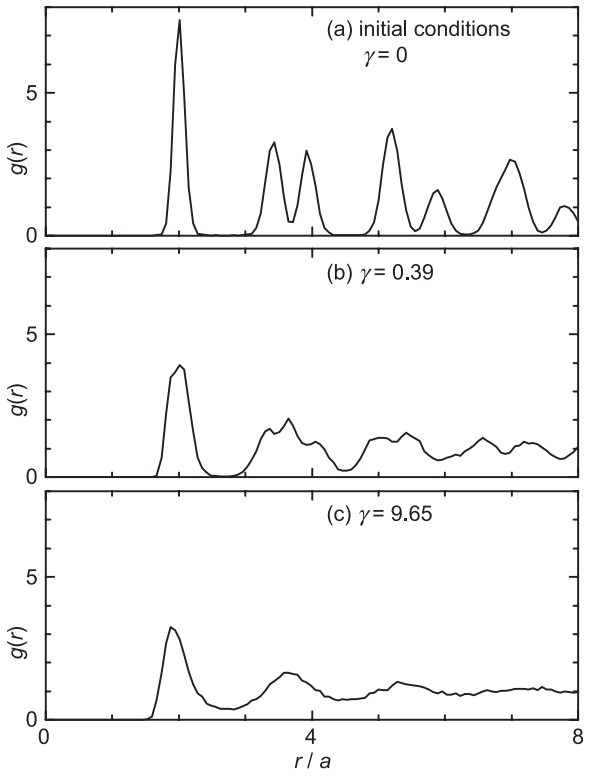

FIG. 3. Pair correlation functions in the gap, at three levels of strain. Initially there is a high degree of spatial order, typical of a crystal, while, at larger forces and strains, the microscopic structure is much more disordered.

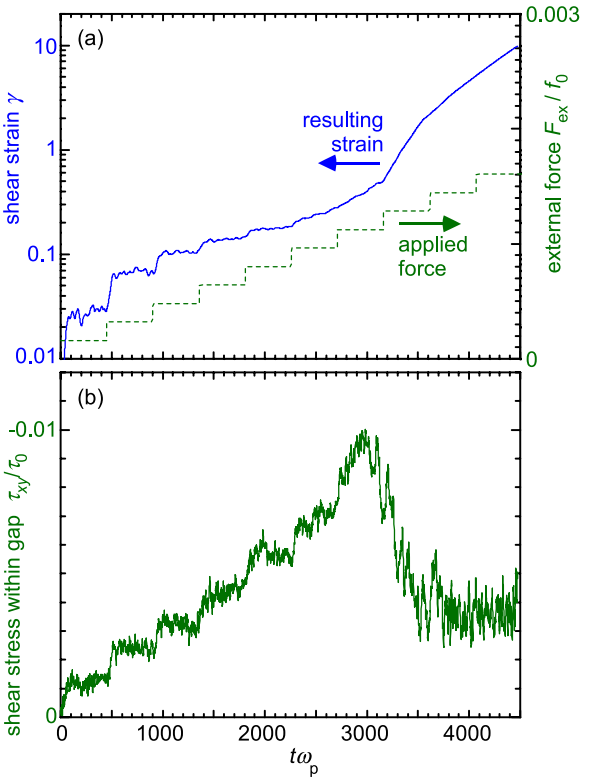

FIG. 4. Time series data. In the simulation, we increased the applied external force $F_{\rm ex}$ in increments, as shown in (a). The resulting shear strain γ and shear stress τ_{xy} are shown in (a) and (b), respectively. For small levels of $F_{\rm ex}$ the deformation was elastic, and the strain γ and stress τ_{xy} remained mostly steady when $F_{\rm ex}$ was steady. At higher levels, the strain and stress were no longer steady, and at still higher levels the stress actually diminished.

mTorr and at room temperature. Under these conditions, the particle motion was under damped, with a characteristic frequency $\omega_p = \sqrt{Q^2/2\pi\epsilon_0 m_p a^3} = 73.9\,\mathrm{s}^{-1}$, which is much larger than the friction constant ν_{gas}.

B. Manipulation

To induce shear motion, we applied two equal but oppositely-directed forces $F_{\rm ex}$, within the shaded rectangular regions in Fig. 2. These external forces, which appear in the last term of Eq. (4), imitate the external manipulation applied by two stripe-shaped laser beams, as in the experiment of Ref. 5. The spatial profile for this force was uniform within the rectangular regions, and the edges were sharp. The central gap between these laser beams had a width of 1.1 mm or $3.9a$.

To allow a determination of the stress-strain relationship, we increased $F_{\rm ex}$ incrementally, as shown in Fig. 4(a). The force was held constant during each of the ten increments, and each had a duration of $452\,\omega_p^{-1}$.

C. Analysis

Our analysis centers on a stress-strain relationship curve. We will use this curve to determine the shear modulus for small strains, and for higher strains, we will use it to obtain the yield stress and a description of the plastic flow. The stress-strain relationship is obtained by calculating stress and strain at different external forces, which were increased in increments during the simulation, to change the levels of strain.

The shear stress is computed inside the central gap as

$$\tau_{xy} = \frac{1}{A}\left[\sum_{j=1}^{M}\frac{\tilde{p}_{jx}\tilde{p}_{jy}}{m_p} - \frac{1}{2}\sum_i\sum_{j\neq i} x_{ij}F_{ij,y}\right], \tag{5}$$

where A and M are the area and number of particles, respectively, in the central gap. The particle momenta $\tilde{p}_{jx}$ and $\tilde{p}_{jy}$ are indicated with a tilde because they represent the fluctuating portion of their momenta, after we have subtracted the local mean flow velocity. The interaction force $F_{ij,y}$ is calculated for each pair of particles i, j as the derivative of the potential energy in Eq. (2). The number of particles M was about 140; this number fluctuated slightly with time, as individual particles moved in and out of the central gap.

The shear strain, which is essentially a transverse gradient of particle displacements, is approximated using a finite difference as

$$\gamma = (X_{\rm top} - X_{\rm bottom})/\Delta y. \tag{6}$$

Here $\Delta y = 7.8a$ is the separation between the top and bottom analysis regions, as marked in Fig. 2; these analysis regions straddle the central gap, and they each have a width $3.9a$. Within the top analysis region, for example, we calculate $X_{\rm top}$ as the x displacement of particles, averaged over all these particles in each time step and then summed over time. Essentially $X_{\rm top}$ and $X_{\rm bottom}$ are accumulated average displacements, in the two analysis regions. For a fixed level

of external forces, one would expect that X_{top} and X_{bottom} to remain steady in the elastic limit, but to increase gradually with time for plastic deformation.

III. RESULTS

Next we present our simulation results, which are in dimensionless units. Length, time, force, and stress are normalized by a, ω_p^{-1}, $f_0 = m_p\omega_p^2 a$, and $\tau_0 = Q^2/4\pi\epsilon_0 a^3$, respectively.

The time series for stress and strain are shown in Fig. 4, as the external force F_{ex} was increased in increments. At low levels of F_{ex}, the conditions in the central gap were elastic, so that the stress and strain were in proportion to the force, and remained steady as long as F_{ex} was fixed. At larger levels, both quantities, strain and stress, were no longer steady, due to the onset of plastic deformation. At still higher levels, the sample made a transition to a liquid; this melting can be identified at $t\omega_p \approx 3000$ in Fig. 4(b) as a decrease in the shear stress, indicating less resistance to flow.

Fluctuations are seen in the stress time series, Fig. 4(b). These fluctuations are possible because we obtain the stress not from the value of the external force F_{ex}, but instead using Eq. (5) based on the motion of a finite number of particles within the central gap. These fluctuations occur even when F_{ex} is constant within an increment, as can be seen in Fig. 4(b). Besides the finite number of particles within the gap, another source of fluctuations in the stress time series could be acoustic waves, emitted far away by events such as a slip at a domain wall.

The data we will use for all our further analysis is the stress-strain relationship, Fig. 5. We obtained this relationship simply by replotting the data from Fig. 4. This relationship shows at least three regimes for shear strain.

A. Elastic deformation

For small strain $\gamma < 0.18$, which we identify as the elastic limit in Fig. 5(b), the stress is proportional to the strain. By fitting the data in this elastic limit to a straight line, we obtain our measured shear modulus G_{2D} as the slope of the line. In physical units, we find $G_{2D} = 4.5 \times 10^{-11}$ Pa m. In dimensionless units, this result is $G_{2D}\tau_0^{-1} = 0.032$.

We can compare our result for the shear modulus to a theoretical shear modulus based on the sound speed of a transverse sound wave. The theoretical expression is $G_{2D} = n_{2D}m_p C_s^2$, where C_s is the transverse sound speed. Calculating C_s using the theory of Ref. 45 for a two-dimensional Yukawa crystal, we obtain $C_s = 0.23a\omega_p = 4.8\,\text{mm s}^{-1}$ for our simulation parameters. For this sound speed, the theoretical shear modulus is $G_{2D}\tau_0^{-1} = 0.034$, which agrees with our simulation result within 6%.

B. Plastic deformation

For somewhat larger strain $0.18 < \gamma < 0.37$ in Fig. 5(b), we find what we identify as the plastic deformation regime. The signature of plastic deformation is that the stress no longer increases with strain the same way as in the elastic limit.

The onset of plastic deformation, i.e., the yield stress, is identified as the point in the stress-strain plot where the two quantities no longer obey the same linear relationship as in the elastic limit. Examining Fig. 5(b) we see that this deviation from the elastic limit occurs at $\gamma = 0.18$. The stress at this point is the yield stress, $\tau_Y = 5.7 \times 10^{-3}\,\tau_0$ or 8.0×10^{-12} Pa m in physical units.

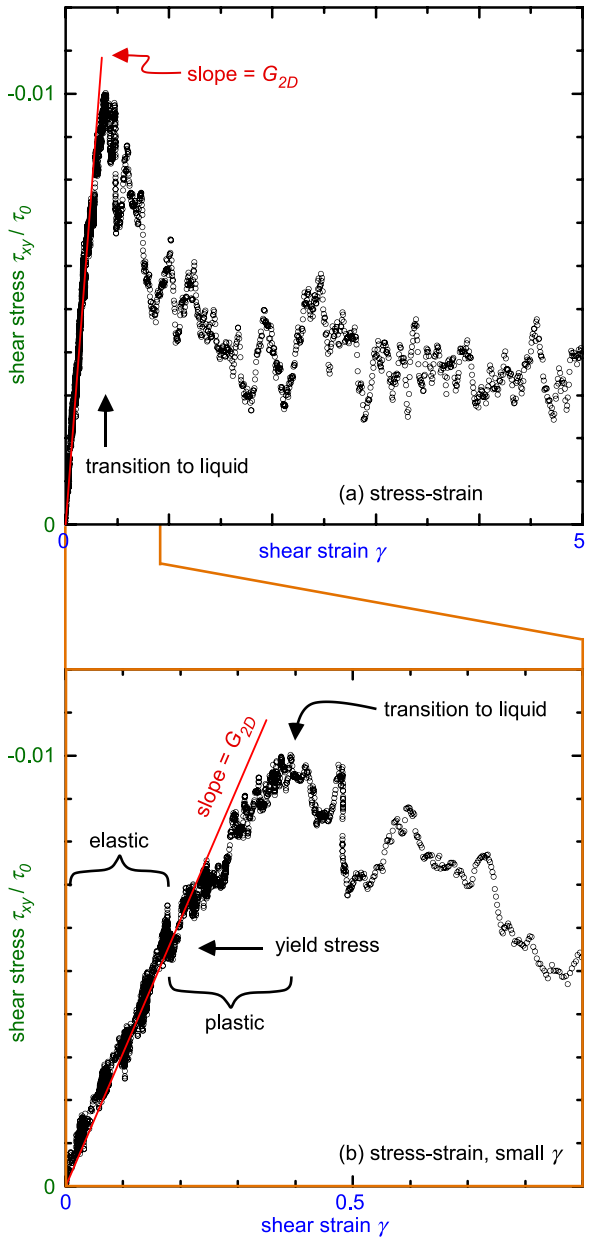

FIG. 5. Stress-strain relationship. The same data are presented in (a) and (b), over different ranges of shear strain. The stress and strain plotted here were obtained from the time series data, Fig. 4. For the elastic portion, we fit the data to a straight line, yielding a slope, as our measurement of the shear modulus G_{2D}. A transition from elastic to plastic deformation, i.e., yield stress, is identified by a change in slope, which is less severe than sketched in Fig. 1(b). A transition to liquids is marked by a maximum shear stress at $\gamma \approx 0.37$. Flow develops at large strain, with an increasing deformation at constant stress.

Our result for the yield stress is quantitatively consistent with a formula for the critical shear stress, based on a theoretical model that is familiar for 3D materials.[43] In physical units, this formula for the theoretical critical shear stress is[43]

$$\tau_{th} = Gb/2\pi h, \tag{7}$$

where G is the shear modulus for 3D materials, b is the particle spacing in the direction of the shear stress, and h is the separation between two neighboring planes that exhibit a dislocation.

To allow a comparison to our result for a 2D substance, we make two substitutes: we use our 2D shear modulus G_{2D} for the 3D shear modulus G, and we use $h = \sqrt{3}b/2$, which is the separation of two adjacent particle rows (parallel to the principal axis) in a 2D triangular lattice. Making these substitutes, we find $\tau_{th} = 5.9 \times 10^{-3}\,\tau_0$, which matches our simulation result $\tau_Y = 5.7 \times 10^{-3}\,\tau_0$ based on Fig. 5(b).

C. Liquid flow

Our stress-strain relationship curve has indications that distinguish three conditions: elastic deformation, plastic flow, and liquid-like flow. The elastic-plastic transition, as mentioned above, is at $\gamma = 0.18$, and it is marked by a deviation from the linear relationship in the low-stress elastic limit. At about double that stress, $\gamma = 0.37$, there is a plastic-liquid transition, which is marked by a peak in the stress. This peak stress is $0.010\tau_0$. Beyond that peak the stress diminished to about one third of the maximum. Furthermore, the microscopic structure in the central gap became more disordered, as indicated by Figs. 3(b) and 3(c), and the flow appeared to be liquid-like, when viewing movies of the particle motion in the simulation. In a future paper, we will analyze the microscopic behavior in the plastic and liquid-like flow regimes.

IV. SENSITIVITY TO TEMPERATURE

Here we assess the sensitivity of shear modulus and yield stress to temperature. To do this, additional simulations were performed at different temperatures. Results are shown in Table I.

We find that both shear modulus and yield stress decrease with temperature. For the temperature range we tested, the decrease is gradual. In Table I, as the temperature increases by a factor of 6, the shear modulus decreases only by 37%, while the yield stress decreases by 63%.

V. SUMMARY

Elastic and plastic deformations of 2D dusty plasma crystal under shear stress were investigated using a simulation. A stress-strain relationship was empirically obtained, by applying two oppositely-directed forces. Based on the stress-strain relationship, we characterize the dusty plasma crystal in three regimes: elastic deformation, plastic deformation, and flow. This characterization results in the shear modulus in the elastic limit and the yield stress at the onset of plastic deformation, for a 2D plasma crystal. The shear modulus from our simulation is found to agree with a theoretical prediction using the speed of transverse sound wave. Our determined yield stress is consistent with a theoretical formula for 3D materials.

TABLE I. Shear modulus and yield stress at different temperatures. Here, temperature is normalized by melting point, $T_{p,m} = 1/\Gamma_m$, where $\Gamma_m = 155$, as determined using the Eq. (4) of Ref. 46 for $\kappa = 0.73$.

Γ	$T_p/T_{p,m}$	Shear modulus G_{2D}/τ_0	Yield stress τ_Y/τ_0
1585	0.1	0.035	0.0078
800	0.2	0.032	0.0057
490	0.3	0.030	0.0056
247	0.6	0.022	0.0048

Experiments may be able to observe the same phenomena; the required observables in an experiment are position and velocity of particles during manipulation by a laser beam, which are standard experimental methods.

ACKNOWLEDGMENTS

We thank Z. Haralson and C.-S. Wong for helpful discussions. This work was supported by NASA and the U.S. Department of Energy.

APPENDIX: COMPARISON WITH OTHER MATERIALS

Here we compare the shear modulus and yield stress for our 2D dusty plasma with that for 2D penta-graphene and typical 3D materials. The latter comparison requires

TABLE II. Comparison with 2D penta-graphene and 3D solid materials. Both the shear modulus and the yield stress are normalized by temperature and number density. The yield data for both penta-graphene and the 3D materials are for tensile yield stress σ_Y, which is $\sqrt{3}$ times larger than the yield stress τ_Y in pure shear, according to the von Mises yield criterion.[47] For 3D materials, the number density is calculated as $n = \rho/m$, where ρ and m are the material's mass density and atomic mass, respectively. Melting point T_m data, not shown here, were from Ref. 48. For 2D penta-graphene, we use $T_m = 4100$ K for melting point[49] and $n_{2D} = 0.453$ Å^{-2} for area density.[50]

				Parameters used for 3D[a]			
3D materials	T/T_m	G/nk_BT	σ_Y/nk_BT	T (K)	G (GPa)	σ_Y (mPa)	ρ (kg/m^3)
Al(refined, 99.98%)	0.31	115	0.04–0.10	298	27.8	10–25	2.7×10^3
Fe(soft, polycrystal)	0.16	239	0.38	298	81.6[b]	131[b]	7.9×10^3
Ag(99.97%)	0.24	125	0.12	293	29.5	28	1.1×10^4
	0.38		0.07	473		25	
	0.55		0.04	673		20	
	0.87		0.02	1073		17	
Sn(single crystal)	0.58	128	0.01	298	19[c]	1.3[c]	7.3×10^3
Au(99.99%)	0.22	110	0.13	298	26	30	1.9×10^4
Lead (cast)	0.49	21	0.02	298	5.54	5.9	1.1×10^4

			Parameters used for graphene[d]	
2D penta-graphene	T/T_m	$\sigma_Y/n_{2D}k_BT$	T (K)	σ_Y(Pa m)
	0.07	119.4	300	22.4
	0.12	68.4	500	21.4
	0.17	39.5	700	17.3

2D dusty plasma	$T_p/T_{p,m}$	$G_{2D}/n_{2D}k_BT_p$	$\tau_Y/n_{2D}k_BT_p$
	0.10	176	38.8
	0.19	80	14.3
	0.32	46	8.6
	0.63	17	3.7

[a]Unless otherwise specified, all parameters data for 3D solids are from Ref. 48.
[b]From Ref. 51.
[c]From Ref. 52.
[d]From Ref. 53.

recasting these quantities in dimensionless units because shear modulus and yield stress have different units in 2D and 3D. Recognizing that this difference in units corresponds to the difference between 2D and 3D number densities, we choose to normalize shear modulus and yield stress by $n_{2D}k_BT$ for 2D and by nk_BT for 3D materials, where n is the 3D number density, and T is the temperature. In Table II, we list the normalized shear modulus and yield stress.

For the normalized shear modulus, we find that a 2D dusty plasma is similar to 3D materials. The normalized shear modulus $G_{2D}/n_{2D}k_BT_p$ is comparable to G/nk_BT for 3D materials, as listed in Table II. The similarity of these two values is possible, despite the very small shear modulus in physical units for the dusty plasma, because the dusty plasma has a very low density n_{2D}.

For the yield stress, we find $\tau_Y/n_{2D}k_BT_p$ for the dusty plasma is comparable to $\sigma_Y/n_{2D}k_BT$ for 2D penta-graphene. However, it is generally larger than σ_Y/nk_BT for 3D materials, by at least one order of magnitude.

[1]G. J. Kalman, P. Hartmann, Z. Donkó, and M. Rosenberg, Phys. Rev. Lett. **92**, 065001 (2004).
[2]Z. Donkó, J. Goree, P. Hartmann, and K. Kutasi, Phys. Rev. Lett. **96**, 145003 (2006).
[3]J. Ashwin and R. Ganesh, Phys. Rev. Lett. **106**, 135001 (2011).
[4]A. Z. Kovács, P. Hartmann, and Z. Donkó, Phys. Plasmas **22**, 103705 (2015).
[5]Z. Haralson and J. Goree, Phys. Rev. Lett. **118**, 195001 (2017).
[6]V. Nosenko and J. Goree, Phys. Rev. Lett. **93**, 155004 (2004).
[7]A. Gavrikov, I. Shakhova, A. Ivanova, O. Petrova, N. Vorona, and V. Fortov, Phys. Lett. A **336**, 378 (2005).
[8]A. V. Gavrikov, D. N. Goranskaya, A. S. Ivanov, O. F. Petrov, R. A. Timirkhanov, N. A. Vorona, and V. E. Fortov, J. Plasma Phys. **76**, 579 (2010).
[9]H. Thomas, G. E. Morfill, V. Demmel, J. Goree, B. Feuerbacher, and D. Mohlmann, Phys. Rev. Lett. **73**, 652 (1994).
[10]J. H. Chu and L. I, Phys. Rev. Lett. **72**, 4009 (1994).
[11]A. Melzer, A. Homann, and A. Piel, Phys. Rev. E **53**, 2757 (1996).
[12]W. T. Juan and I. Lin, Phys. Rev. Lett. **80**, 3073 (1998).
[13]B. Liu, J. Goree, V. Nosenko, and L. Boufendi, Phys. Plasmas **10**, 9 (2003).
[14]O. Ishihara, J. Phys. D: Appl. Phys. **40**, R121 (2007).
[15]A. Melzer and J. Goree, in *Low Temperature Plasmas: Fundamentals, Technologies and Techniques*, 2nd ed., edited by R. Hippler, H. Kersten, M. Schmidt, and K. H. Schoenbach (Wiley-VCH, Weinheim, 2008), p. 129.
[16]G. E. Morfill and A. V. Ivlev, Rev. Mod. Phys. **81**, 1353 (2009).
[17]M. Bonitz, C. Henning, and D. Block, Rep. Prog. Phys. **73**, 066501 (2010).
[18]S. Jaiswal, P. Bandyopadhyay, and A. Sen, Plasma Sources Sci. Technol. **25**, 065021 (2016).
[19]C.-R. Du, K. R. Sütterlin, K. Jiang, C. Räth, A. V. Ivlev, S. Khrapak, M. Schwabe, H. M. Thomas, V. E. Fortov, A. M. Lipaev, V. I. Molotkov, O. F. Petrov, Y. Malentschenko, F. Yurtschichin, Y. Lonchakov, and G. E. Morfill, New J. Phys. **14**, 073058 (2012).
[20]G. J. Kalman, S. Kyrkos, K. I. Golden, P. Hartmann, and Z. Donko, Contrib. Plasma Phys. **52**, 219 (2012).
[21]C. M. Ticoş, D. Toader, M. L. Munteanu, N. Banu, and A. Scurtu, J. Plasma Phys. **79**, 273 (2013).
[22]T. Ott, M. Stanley, and M. Bonitz, Phys. Plasmas **18**, 063701 (2011).
[23]U. Konopka, G. E. Morfill, and L. Ratke, Phys. Rev. Lett. **84**, 891 (2000).
[24]J. Kong, K. Qiao, L. S. Matthews, and T. W. Hyde, Phys. Rev. E **90**, 013107 (2014).
[25]K. Qiao, J. Kong, L. S. Matthews, and T. W. Hyde, Phys. Rev. E **91**, 053101 (2015).
[26]Y. Feng, J. Goree, and B. Liu, Phys. Rev. Lett. **109**, 185002 (2012).
[27]H. M. Lindsay and P. M. Chaikin, J. Chem. Phys. **76**, 3774 (1982).
[28]M. Y. Pustylnik, M. A. Fink, V. Nosenko, T. Antonova, T. Hagl, H. M. Thomas, A. V. Zobnin, A. M. Lipaev, A. D. Usachev, V. I. Molotkov, O. F. Petrov, V. E. Fortov, C. Rau, C. Deysenroth, S. Albrecht, M. Kretschmer, M. H. Thoma, G. E. Morfill, R. Seurig, A. Stettner, V. A. Alyamovskaya, A. Orr, E. Kufner, E. G. Lavrenko, G. I. Padalka, E. O. Serova, A. M. Samokutyayev, and S. Christoforetti, Rev. Sci. Instrum. **87**, 093505 (2016).
[29]C. Durniak and D. Samsonov, Phys. Rev. Lett. **106**, 175001 (2011).
[30]V. Nosenko, A. V. Ivlev, and G. E. Morfill, Phys. Rev. Lett. **108**, 135005 (2012).
[31]C. Durniak, D. Samsonov, J. F. Ralph, S. Zhdanov, and G. Morfill, Phys. Rev. E **88**, 053101 (2013).
[32]P. Hartmann, A. Z. Kovács, A. M. Douglass, J. C. Reyes, L. S. Matthews, and T. W. Hyde, Phys. Rev. Lett. **113**, 025002 (2014).
[33]C. Yang, W. Wang, and I. Lin, Phys. Rev. E **93**, 013202 (2016).
[34]V. Nosenko, A. V. Ivlev, and G. E. Morfill, Phys. Rev. E **87**, 043115 (2013).
[35]C.-L. Chan and I. Lin, Phys. Rev. Lett. **98**, 105002 (2007).
[36]C.-L. Chan, W.-Y. Woon, and I. Lin, Phys. Rev. Lett. **93**, 220602 (2004).
[37]P. Hartmann, M. C. Sándor, A. Kovács, and Z. Donkó, Phys. Rev. E **84**, 016404 (2011).
[38]B. Liu, Y.-H. Liu, Y.-P. Chen, S.-Z. Yang, and L. Wang, Chin. Phys. **12**, 765 (2003).
[39]D. Howell, R. P. Behringer, and C. Veje, Phys. Rev. Lett. **82**, 5241 (1999).
[40]J. Ren, J. A. Dijksman, and R. P. Behringer, Phys. Rev. Lett. **110**, 018302 (2013).
[41]N. Y. C. Lin, M. Bierbaum, P. Schall, J. P. Sethna, and I. Cohen, Nat. Mater. **15**, 1172 (2016).
[42]S. E. Spagnolie, *Complex Fluids in Biological Systems* (Springer, New York, 2015).
[43]P. Oswald, *Rheophysics: The Deforamtion and Flow of Matter* (Cambridge, New York, 2009).
[44]B. Liu and J. Goree, Phys. Plasmas **23**, 073707 (2016).
[45]X. Wang, A. Bhattacharjee, and S. Hu, Phys. Rev. Lett. **86**, 2569 (2001).
[46]P. Hartmann, G. J. Kalman, Z. Donkó, and K. Kutasi, Phys. Rev. E **72**, 026409 (2005).
[47]W. F. Hosford, *Solid Mechanics* (Cambridge University Press, New York, 2010).
[48]*Springer Handbook of Condensed Matter and Materials Data*, edited by W. Martienssen and H. Warlimont (Springer, New York, 2005).
[49]S. W. Cranford, Carbon **96**, 421 (2016).
[50]H. Sun, S. Mukherjee, and C. V. Singh, Phys. Chem. Chem. Phys. **18**, 26736 (2016).
[51]F. Cardarelli, *Materials Handbook: A Concise Desktop Reference* (Springer-Verlag, London, 2008).
[52]C. Kittel, *Introduction to Solid State Physics*, 8th ed. (John Wiley & Sons, Inc, Hoboken, NJ, 2005).
[53]M.-Q. Le, Comput. Mater. Sci. **136**, 181 (2017).